Catalysis Today 166 (2011) 10–17

Contents lists available at ScienceDirect

Catalysis Today

journal homepage: www.elsevier.com/locate/cattod

Raman spectroscopy and X-ray diffraction study of the phase transformation of ZrO_2–Al_2O_3 and CeO_2–Al_2O_3 nanocomposites

Sara Boullosa-Eiras, Estelle Vanhaecke, Tiejun Zhao, De Chen*, Anders Holmen

Department of Chemical Engineering, Norwegian University of Science and Technology, Sem Sælands Vei 4, N-7493 Trondheim, Norway

ARTICLE INFO

Article history:
Available online 7 July 2010

Keywords:
Ceria
Zirconia
X-ray diffraction
Alumina
Raman spectroscopy

ABSTRACT

Combined UV Raman spectroscopy using radiation of 325 nm, visible Raman spectroscopy excited by 633 nm laser, X-ray diffraction and nitrogen adsorption–desorption surface area measurements were used in the present work to investigate the mechanism of the phase transformation and sintering of ZrO_2–Al_2O_3 and CeO_2–Al_2O_3 nanocomposites synthesized by a nanoparticle-mediated Pechini sol–gel method. These materials were compared to pure alumina, ZrO_2 and CeO_2 nanoparticles calcined at different temperatures. The modification of the alumina surface with CeO_2 and ZrO_2 can significantly delay the phase transformation and sintering. UV Raman spectroscopy is found to be more sensitive at the surface region for the ZrO_2–Al_2O_3 and CeO_2–Al_2O_3 nanocomposites, making possible to study the phase changes of the additional oxide. A synergetic stabilization effect between two oxides such as Al_2O_3 and ZrO_2 or CeO_2 was found, where the phase transformation and sintering of both oxides were delayed. The results reveal the role of the second oxides in the nanocomposites in suppressing surface-mediated sintering thus gaining a higher stability of the materials at high temperatures.

1. Introduction

Alumina is considered one of the most important and used ceramics in different field of applications such as catalyst supports, in electronic-device fabrication, as a protective or buffer layer against corrosion or also as an alternative for surgical materials for implants [1,2]. The most stable state of alumina is α-alumina, but it also presents different metastable structures like γ, δ or also θ-phase. These metastable aluminas have partially disordered crystal structures based on closed packed oxygen sublattice with varying interstitial aluminium configurations. As equilibrium is approached the structures become more ordered by forming a hexagonal oxygen sublattice until α-alumina is formed [3]. The main difference between the phases can be explained by the distribution of oxygen sublattice into the interstitial sites. For example, the α-Al_2O_3 is particularly stable thanks to the selective position of oxygen sublattice in octahedral sites instead of being in both tetrahedral and octahedral sites as in the case of the metastable phases [3]. The crystal structure of the different alumina phases identified in our samples is presented in Table 1.

However, applications taking place at high temperatures require even a more high-temperature stable support. The specific surface area of alumina deteriorates remarkably above 1000 °C owing to sintering and phase transition to α-alumina. It has been proposed that the alumina particle growth occurs by elimination of water from hydroxyl groups adsorbed on two adjacent particles resulting in new Al–O–Al bonds. Additives reduce the possibility of loss of surface area by replacing the hydroxyl groups [4].

As an example, CeO_2–Al_2O_3 nanocomposites have been frequently used as part of the formulation of the Three-Way-Catalysts [5–7]. The main problem and challenge remains in the preparation and characterization of such supported oxides in keeping a stable phase of the oxides which could be also resistant to sintering problems [7]. In addition, ZrO_2–Al_2O_3 composites have improved mechanical properties compared with Al_2O_3 or ZrO_2 alone [7–9]. When oxides such as CeO_2 and ZrO_2 are used to modify the alumina, a synergic thermal stability effect on both materials is possible [7,10–17].

X-ray diffraction (XRD) has often been used for the study of the alumina phase transitions [1], but due to the fact that several alumina phases are present when the powder is subjected to heat treatment, the employment of other characterization tools is useful for validation of the results. The use of techniques such as Infrared (IR) or Raman spectroscopy has been previously reported for identifying the aluminium hydroxide phases due to differences in the hydroxyl stretching region [1,16–19].

Combined techniques including UV Raman spectroscopy using radiation of 325 and 244 nm, visible Raman spectroscopy excited by 633 nm laser, X-ray diffraction (XRD) and transmission electron

---

* Corresponding author.
E-mail addresses: chen@chemeng.ntnu.no (D. Chen), anders.holmen@chemeng.ntnu.no (A. Holmen).

0920-5861/$ – see front matter © 2010 Elsevier B.V. All rights reserved.
doi:10.1016/j.cattod.2010.05.038

Table 1
Crystallographic data for different aluminas [3].

	δ-Al_2O_3	θ-Al_2O_3	α-Al_2O_3
Crystal system	Tetragonal	Monoclinic	Rhombohedral
Space group	*P*–4*m*2	*A*2/*m*	*R*3*c*
Lattice parameters			
a	7.94	5.62	4.76
b		2.91	
c	23.5	11.79	12.99
β		103.74	

microscopy (TEM) have been recently approved to be a very powerful tool to gain a better understanding of the phase transformation and sintering mechanism of oxide materials [20,21]. UV Raman spectroscopy is found to be more sensitive to the surface region phase of a solid sample when the sample absorbs UV light [20,21]. Li and co-workers have studied the phase transformation of zirconia (ZrO_2) [20,21] and titania (TiO_2) [22,23] by these combined techniques. They clearly indicated that the surface phase of the oxides is usually different from the bulk phase of ZrO_2. They have demonstrated that the hysteresis of outer phase transformation of TiO_2 is common for the phase transformation of nanoparticles. They have also developed an interface/bulk nucleation mechanism to reasonably interpret the distinct phenomena during the TiO_2 phase transformation with different particle sizes. Based on this theory, they have successfully developed a method of surface modification by a oxide to reduce the sintering [23]. The combined techniques have been found powerful to understand the catalyst structure and the correlation between the surface properties and the catalytic activity of nanooxides [24,25].

Although it has long been recognized that the mechanism of alumina sintering involves phase transfer and α-alumina nucleation and growth at θ/α interface [26], a better understanding of the phase transfer could be gained by a detailed investigation using combined techniques. It may serve as a solid fundamental for the rational design of materials with a much better thermal stability.

In the present work, combined techniques by using UV Raman spectroscopy with laser excitation at 325 nm laser, visible Raman spectroscopy with laser excitation at 633 nm laser, XRD and BET surface area measurement are used to investigate the mechanism of the phase transformation and sintering of ZrO_2–Al_2O_3 and CeO_2–Al_2O_3 nanocomposites synthesized by a nanoparticle-mediated Pechini sol–gel method. Those materials are compared to pure alumina, ZrO_2 and CeO_2 nanoparticles calcined at different temperatures to reveal a mechanism for gaining a higher stability of the nanocomposites at high temperatures.

2. Experimental

A nanoparticle-mediated Pechini sol–gel method [27,28] was employed for the preparation of the different nanocomposites to ensure a better surface contact between one oxide nanoparticles with a second oxide. Zirconium and cerium precursors ($ZrO(NO_3)_3 \cdot xH_2O$ (37.5 wt.% ZrO_2) and $Ce(NO_3)_3 \cdot 6H_2O$ respectively), were introduced to modify the alumina surface. Typically, ZrO_2/CeO_2–Al_2O_3 (the CeO_2 or ZrO_2 weight fraction is 20%) was prepared as follows: citric acid was used to obtain a complex of the metal precursor. When adding polyethylene glycol (PEG) (0.1 g/mL water) a homogeneous polymeric matrix was produced. Afterwards, the alumina powders (Puralox 200, Sasol) were stepwise dropped into the former solution, to produce a suspension under vigorous stirring. The water was gradually removed by evaporation at 85 °C to form a dried solid. Different calcination temperatures between 900 and 1200 °C, with a calcination time of 5 h, were employed for testing the thermal stability of the materials, and to study the phase transformation of both alumina and the additional metal oxides. For the sake of comparison, single metal oxides such as ZrO_2 and CeO_2 were prepared using the similar procedure without adding the alumina powder into the complex solution.

Raman spectra were collected on a Horiba Jobin Yvon LabRAM HR800 spectrometer. The emission lines at 633 nm from a He–Ne laser and 325 nm from He–Cd were focused on the sample with a 100× objective. No filter was used during the measurements. The UV Raman is particularly appreciated to overcome fluorescence, which is very often present for alumina powder and also to increase the sensitivity especially at the surface region [29].

X-ray diffraction (XRD) patterns were recorded at room temperature on a Bruker AXS D8 Focus diffractometer using Cu Kα radiation ($\lambda = 1.54$ Å). The X-ray tube voltage was set to 40 kV and the current to 50 mA. XRD patterns were collected in the range of 2θ from 20° to 85°, at 0.01°/step with integration times of 1 s/step. The solid phases in XRD patterns were identified by comparing with standards in a database to identify the phases. The crystal size analysis of the solid from XRD patterns were calculated using the TOPAS program based on the Pawley method [30]. The value based in the integral breath (IB) was used in this study. The unit cell details such as space group and the unit cell parameters for each of the phases present in the sample were introduced in the TOPAS program for linking the several peaks present. The crystal size was calculated by taking into account each of the peaks related to each phase. The fitting was done using the fundamental parameters approach, which employs the geometry of the diffractometer together with other information to model the contribution to the peak profiles.

Nitrogen adsorption–desorption isotherms of the samples were measured with a Micromeritics TriStar 3000 instrument, and the data were collected at liquid nitrogen temperature, 77 K. The samples were outgassed at 473 K overnight prior to measurement. The surface area was calculated from the Brunauer–Emmett–Teller (BET) equation.

3. Results and discussion

3.1. X-ray diffraction and Raman study of the alumina support

The combination of techniques such as XRD, visible and UV Raman spectroscopy helps to identify the phase transitions of the alumina sample. Fig. 1a–c shows the XRD patterns, visible and UV Raman spectra, for the alumina samples calcined for 5 h at temperatures between 900 and 1200 °C, respectively.

The high fluorescence of the δ-phase makes its determination complicated by Raman spectroscopy, because it is present as a background which is covered by the peaks related to the θ-phase as shown in Fig. 1c. In contrast, the results from XRD and visible Raman spectroscopy in Fig. 1a and b suggest that after calcination at 900 °C for 5 h, the tetragonal δ-Al_2O_3 structure is dominant in the alumina samples. When the sample is calcined at 1000 °C for 5 h, the coexistence of δ and θ-Al_2O_3 is observed in Fig. 1a, whereas no obvious patterns of α-Al_2O_3 appear in the XRD diffractogram. Furthermore, under the same condition, visible Raman spectroscopy in Fig. 1b shows that two peaks appear at 1176 and 1242 cm^{-1}, probably related to the θ-Al_2O_3, implying that the θ-Al_2O_3 has response to visible Raman spectra. However, no obvious peaks of this phase exist in the UV Raman spectroscopy in Fig. 1c due to the very weak UV adsorption of θ-Al_2O_3. It should be noticed that two new but very weak Raman bands at 1370 and 1397 cm^{-1} are observed in the visible Raman spectroscopy, implying another phase already appears under this calcination condition.

When the calcination temperature is raised to 1100 °C, the differences in the spectra are found between XRD, visible and UV Raman spectroscopy patterns in Fig. 1a–c. XRD patterns in

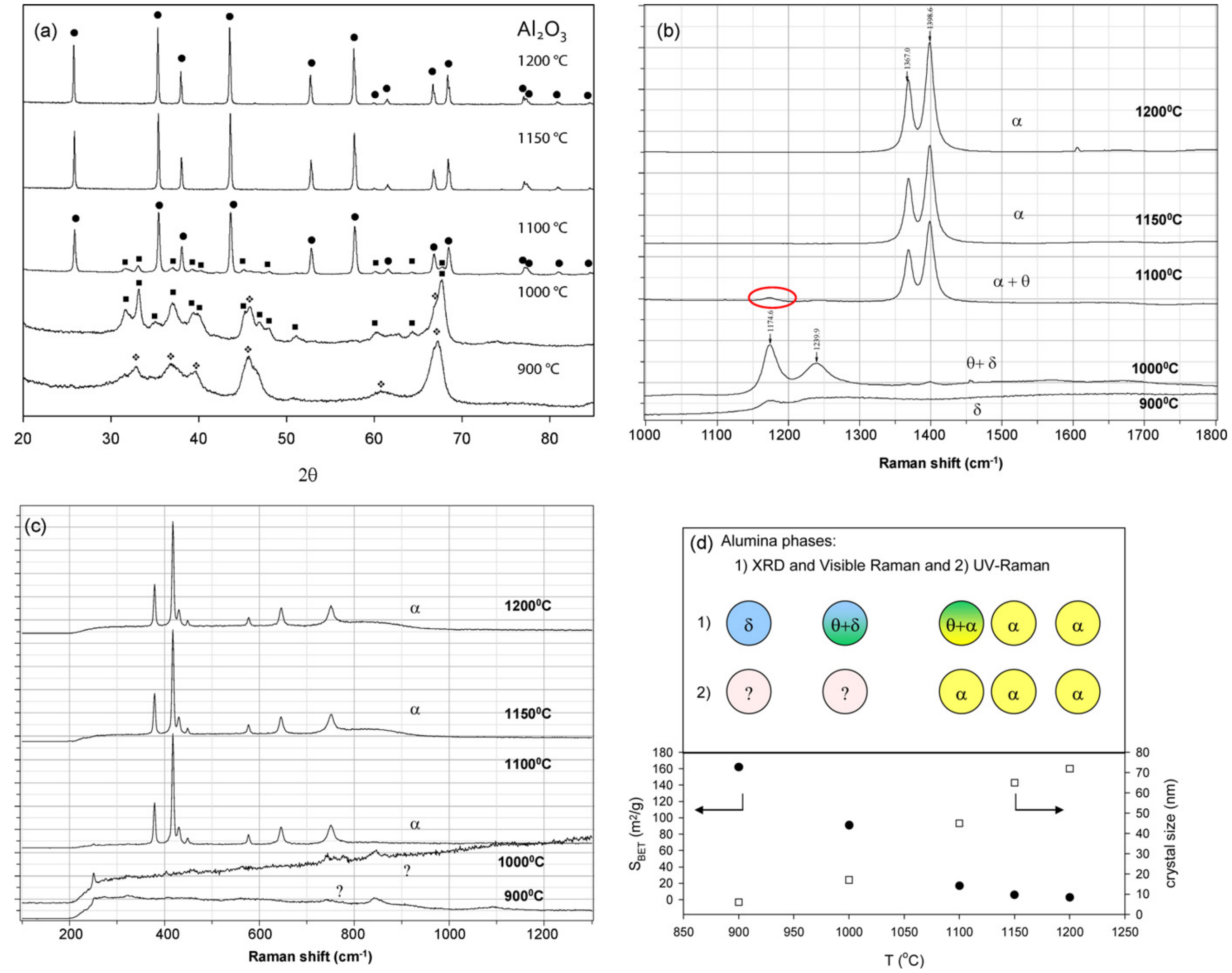

Fig. 1. (a) XRD diffratograms for the alumina calcined at temperatures between 900 and 1200 °C. Data collected at 0.02°/step between $2\theta = 25°$ and 85° (●, α-Al_2O_3; ■, θ-Al_2O_3; ❖, δ-Al_2O_3). (b) Vis-Raman results for the alumina calcined at temperatures between 900 and 1200 °C by 5 h. Spectrum recorded at 633 nm in the Raman shift interval between 1000 and 1800 cm^{-1}. (c) UV-raman spectra of the alumina calcined at temperatures between 900 and 1200 °C by 5 h. Spectrum recorded at 325 nm in the Raman shift interval between 100 and 1300 cm^{-1}. (d) Comparison of the surface area (●) values with the alumina crystal size (□) for the different calcination temperatures. Results are compared with the different phases observed according to XRD and visible Raman (1) and UV-Raman (2) at each of the temperatures.

Fig. 1a exhibit the typical spectra for α-Al_2O_3 with sharp peaks, indicating a well-defined crystal structure in this material under this heat treatment. Meanwhile, the θ-Al_2O_3 is still observed as noticed in Fig. 1a. Under the same conditions, visible Raman spectroscopy in Fig. 1b exhibits two new and strong Raman bands at 1370 and 1397 cm^{-1} and the weaker Raman bands at 1176 and 1242 cm^{-1} compared with the spectra at 1000 °C. By combination with XRD measurements, those latter peaks might be attributed to the phase transformation from θ-Al_2O_3 to α-Al_2O_3. XRD and visible Raman spectroscopy give similar structural information about the material under this condition, consistent with the observation proposed by Li [20,21]. However, from our observation, as the previous paragraph described, the Raman bands at 1370 and 1397 cm^{-1} already appeared when the sample is heat treated at 1000 °C, indicating that the very small amount of α-Al_2O_3 already exist. This observation could be related to the fact that visible Raman spectroscopy is more sensitive to the phase transformation than XRD, since in the latter case, a long range order is needed, whereas the former is responsible for band change. All the θ-Al_2O_3 are converted to α-Al_2O_3 at calcination temperature of 1150 °C.

UV Raman spectroscopy gives strong Raman bands response for the sample calcined at 1100 °C as shown in Fig. 1c. Combined the results from XRD and visible Raman spectroscopy, these strong Raman bands are due to the formation of α-Al_2O_3, indicating the fact that UV Raman spectroscopy is very sensitive to the existence of α-Al_2O_3. With the increased heat treatment to 1150 and 1200 °C, the appeared peaks in the XRD pattern and visible Raman spectra, shown in Fig. 1a and b, respectively, are identified as α-Al_2O_3. The increased intensity of the peaks implies a better crystal structure with the temperature.

Due to UV Raman spectroscopy is only sensitive to the α-Al_2O_3, while θ-alumina weakly absorb UV laser light as shown in the literature [31]. Hence, UV Raman spectroscopy cannot be used to observe the entire phase transformation from θ-Al_2O_3 to α-Al_2O_3.

The results of XRD, BET and Raman spectroscopy for the alumina samples with the different temperature treatment are summarized in Fig. 1d. The information of alumina phase at different corresponding calcination temperatures are presented on the top of the figure. The circles labelled with (1) give the results from XRD and visible Raman spectroscopy. The circles labelled with (2) summarize the results from UV Raman spectroscopy. When two alumina phases exist in the same sample, the crystal size is presented by using the corresponding phase with larger value. As expected, when the α-phase is formed at 1100 °C, the alumina crystal size increases and the surface area decreases dramatically. Based on the interface nucleation theory [23], the α-Al_2O_3 nucleates first on the particle surface as revealed above. This α-alumina could possibly be in contact with unconverted θ-Al_2O_3 to form θ/α interface for the particle growth [26]. The substantial decrease of the surface area and the formation of α-Al_2O_3 can lead to poor surface reactivity and mechanical strength, which should be avoided in the reaction system, especially at high-temperature condition. Introducing a second oxide is a possible strategy to prevent the formation of α-Al_2O_3.

3.2. Al_2O_3 phase transformation on the ZrO_2–Al_2O_3 and CeO_2–Al_2O_3 composites

To investigate the effect of the second oxide such as CeO_2 and ZrO_2 on the thermal stability of the Al_2O_3-based composite, in this study, the modified Pechini method is used by impregnation of the Zr- or Ce- citrate- PEG complex solution into the Al_2O_3 powder through a simple evaporation-drying procedure. The resulting powdered solids are then calcined at temperatures between 900 and 1200 °C to obtain the nanocomposite. Figs. 2a and 3a give the visible Raman spectra for the calcined ZrO_2–Al_2O_3 and CeO_2–Al_2O_3, while Figs. 2b and 3b give the XRD patterns for these nanocomposites, respectively.

The phase transition to α-Al_2O_3 in the alumina sample alone can be obviously observed when the sample is calcined at 1100 °C for 5 h as presented in the previous section (Fig. 1a–c). In contrast, very small peaks in the XRD pattern for α-Al_2O_3 appear in the ZrO_2–Al_2O_3 composite calcined at the same conditions as shown in Fig. 2b, whereas the peaks for θ-Al_2O_3 and t-ZrO_2 can be obviously observed. When the calcination temperature increases to 1150 °C, noticeable peaks for α-Al_2O_3 can be found in the composite, although no obvious decrease of the peak intensity for θ-Al_2O_3, indicating that the fraction of α-Al_2O_3 in the composite is small that the fraction of. Furthermore increasing the calcination temperature to 1200 °C, the peaks for θ-Al_2O_3 disappear, and only the ones for α-Al_2O_3 and ZrO_2 can be observed. Similar results for the formation of α-Al_2O_3 can be obtained for CeO_2–Al_2O_3 after calcination between 900 and 1200 °C, as presented in Fig. 3b.

The visible Raman spectra for these two composites in Figs. 2a and 3a give similar results for the formation of α-Al_2O_3; Raman peaks for α-Al_2O_3 are observed together with the peaks for θ-Al_2O_3 at 1100 °C for ZrO_2–Al_2O_3. However, compared with the Al_2O_3 alone in Fig. 1b, the peak intensity of α-Al_2O_3 is significantly lower. Substantial peaks for θ-Al_2O_3 still can be observed when the sample is calcined at 1150 °C for 5 h.

From these observations by XRD and visible Raman spectroscopy, adding the second oxide in the Al_2O_3 can effectively increase the calcination temperature about 100 °C for the formation of α-Al_2O_3 compared with the Al_2O_3 sample alone.

In addition, it is found that in the case of the composite after introducing the ZrO_2 or CeO_2 into Al_2O_3, the signal related to the α-Al_2O_3 in UV Raman spectroscopy completely disappears as typically shown in Fig. 4a for the case of ZrO_2–Al_2O_3, whereas α-Al_2O_3 alone have strong response in the UV Raman spectroscopy as shown in Fig. 1c. There are several possibilities for this observation: formation of the new compound between the ZrO_2 and Al_2O_3 rather than α-Al_2O_3; blockage of the response to UV Raman bands of α-Al_2O_3 in the composite preventing the formation of α-Al_2O_3. However, those possibilities can be excluded by the clear peaks appearing for α-Al_2O_3 in the XRD and visible Raman spectroscopy.

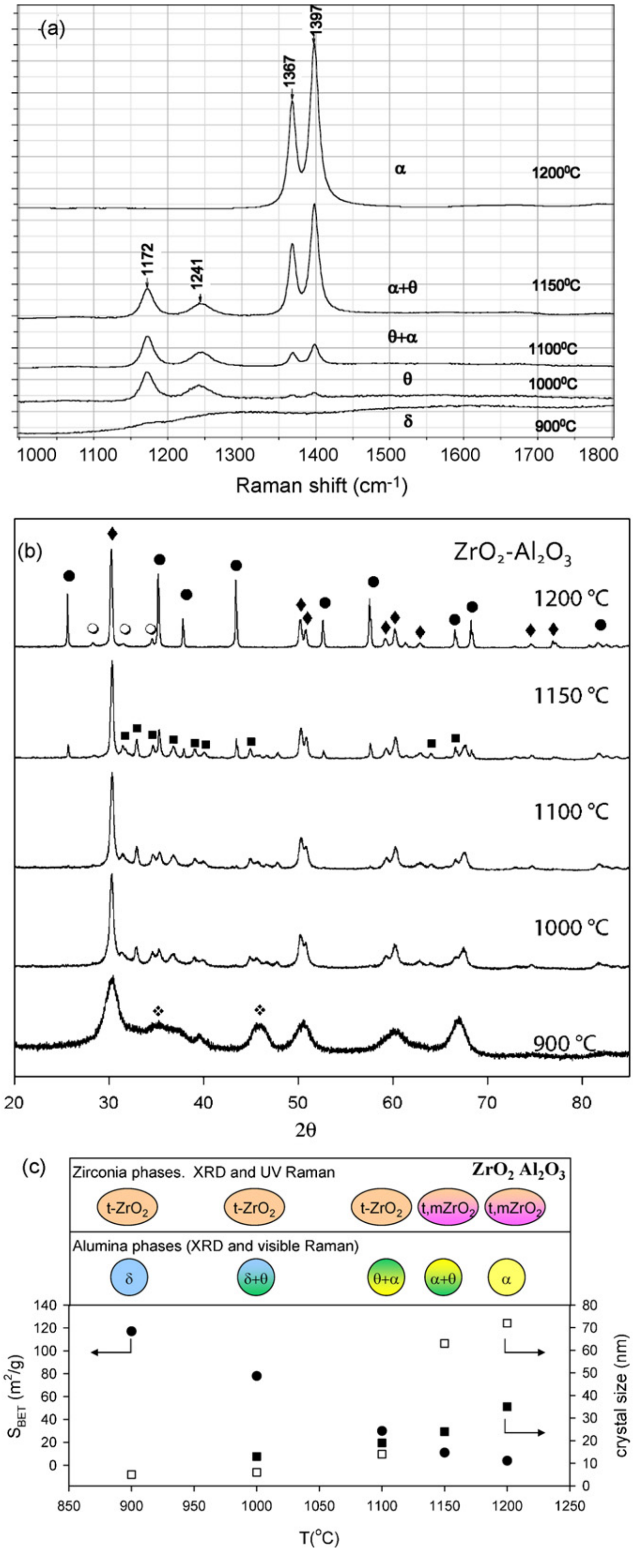

Fig. 2. (a) Visible Raman results for Al_2O_3 phases in the ZrO_2–Al_2O_3 nanocomposite calcined at temperatures between 900 and 1200 °C. Spectrum recorded at 633 nm in the Raman shift interval between 1000 and 1800 cm^{-1}. (b) XRD diffractograms for the ZrO_2–Al_2O_3 nanocomposite calcined at different temperatures. Data collected at 0.02°/step between $2\theta = 25°$ and 85° (♦, t-ZrO_2; ○, m-ZrO_2; ●, α-Al_2O_3; ■, θ-Al_2O_3; ❖, δ-Al_2O_3). (c) Comparison of the surface area (●) values with the crystal size for alumina (□) and zirconia (■) for the different calcination temperatures. Results are compared with the different phases observed according XRD and Raman.

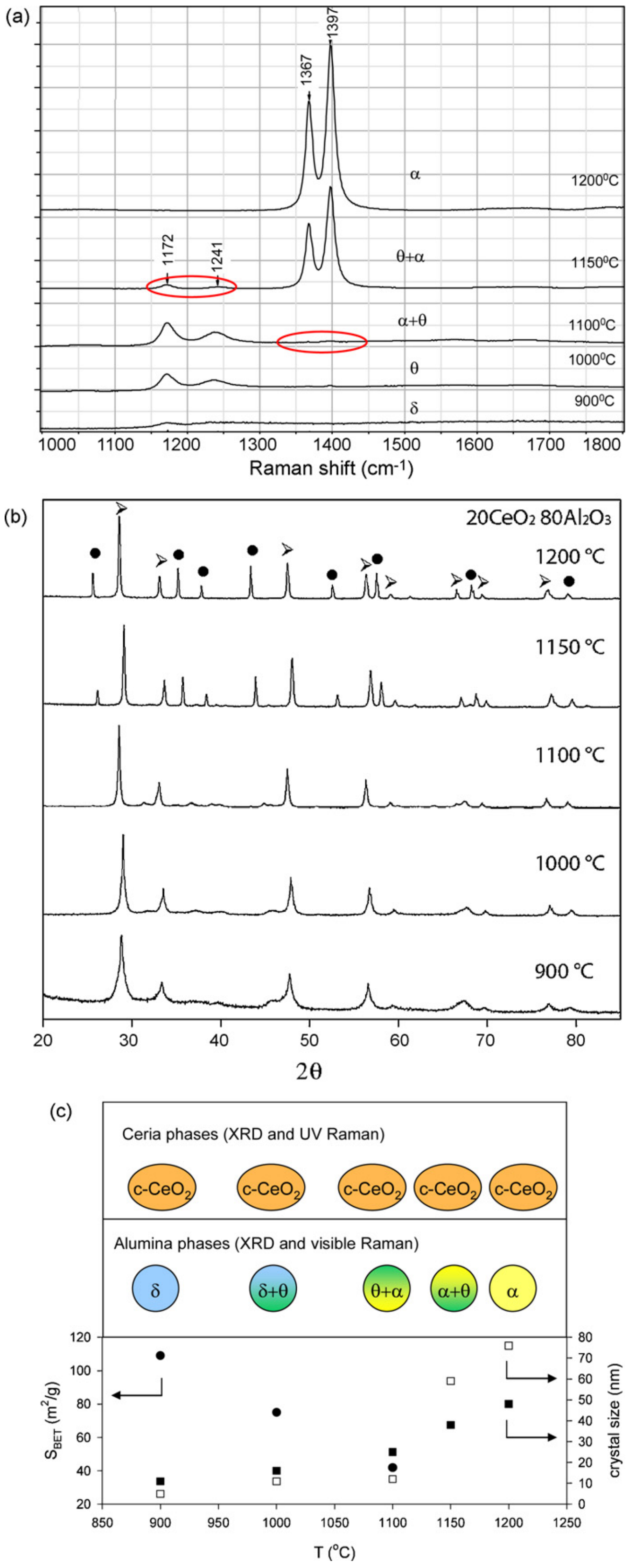

Fig. 3. (a) Visible Raman results for Al_2O_3 phases in the CeO_2–Al_2O_3 nanocomposite calcined at temperatures between 900 and 1200 °C. Spectrum recorded at 633 nm in the Raman shift interval between 1000 and 1800 cm^{-1}. (b) XRD diffractograms for the CeO_2–Al_2O_3 nanocomposite calcined at different temperatures. Data collected at 0.02°/step between $2\theta = 25°$ and 85° (➤, c-CeO_2; ●, α-Al_2O_3; ■, θ-Al_2O_3; ❖, δ-Al_2O_3). (c) Comparison of the surface area (●) values with the crystal size for alumina (□) and ceria (■) for the different calcination temperatures. Results are compared with the different phases observed according to XRD and Raman. c-ceria is found in the whole temperature range according to both techniques.

According to Li investigations [20–23], UV-Raman spectroscopy is a surface region sensitive technique when the material absorbs UV light as they demonstrated for ZrO_2 or TiO_2, where the Raman bands under UV emission are only responsible for the surface species due to the adsorption of UV light and subsequently scattering light in the bulk phase. Therefore, the absence of Raman bands for α-Al_2O_3 could be related to the formation of an oxide layer on alumina, forming a core shell Al_2O_3 @ZrO_2 structure. This possibility lies in the expectation from the preparation procedure of the nanoparticle-mediated Pechini sol–gel method, where the citrate complex can react with the OH group on the Al_2O_3 surface, thus giving a covering of polymeric layers on the surface of Al_2O_3. These produced oxides after calcinations can closely interact with the alumina, and block the defects which are a typical surface nucleation site. As a result, it increases the energy barrier for surface nucleation and thus delaying the phase transformation of Al_2O_3 at high temperature. More importantly, it blocks the pathway to form the θ/α interface for the particle growth [26] as in the pure alumina sample. Then, it might reduce the potential for sintering and retain a higher surface area in the nanocomposite.

3.3. *ZrO_2 phases in ZrO_2–Al_2O_3 nanocomposites and ZrO_2 nanoparticles*

ZrO_2 exists in three different phases namely monoclinic, tetragonal and cubic [20,32–34]. Mainly previous works were reporting the doping of ZrO_2 structures in order to stabilize the tetragonal phase and to prevent the sintering of the nanoparticles. Fig. 4a shows a comparison of the UV Raman spectra of the nanocomposites and zirconia samples prepared by the Pechini method calcined at temperatures in the interval of 900–1200 °C. The nanocomposites (in dashed line) show mainly peaks at 270, 316, 459 and 640 cm^{-1} which are related to the tetragonal phase after calcination at 900, 1000 and 1100 °C [20,32,35,36]. Besides, variations are observed in the UV Raman spectra at a calcination temperature of 1150 °C, two new peaks appear at 380 and 418 cm^{-1} which confirm the presence of the monoclinic phase (m-ZrO_2) after this thermal treatment [20,36]. This observation is consistent with the XRD results showed in Fig. 2b: with the increased calcination temperature to 1150 °C, two new peaks emerge from 1150 °C at 29° and 31.5°. Those peaks are identified as the presence of m-ZrO_2. Since UV Raman spectroscopy is more sensitive to the surface in this case, it seems that the monoclinic phase appears at the surface only at 1150 °C, since no obvious XRD peaks related to the m-ZrO_2 under this condition, whereas significant Raman peaks are already found. For the sample calcined at 1200 °C, both the XRD and UV Raman spectroscopy give the information about the formation of m-ZrO_2: the Raman bands at 380 and 418 cm^{-1} are detected for m-ZrO_2 in the nanocomposites and specific peaks for m-ZrO_2 are identified in the corresponding XRD in Fig. 2b.

A comparison between a single ZrO_2 sample and the ZrO_2–Al_2O_3 nanocomposite sample is carried out by using UV Raman spectroscopy and XRD in Fig. 4a and b, and analyzed results are summarized in Fig. 4c. The dashed spectrum corresponds to ZrO_2 and the solid one is ZrO_2–Al_2O_3. As seen in Fig. 4a differences under UV laser are clearly noticeable between both: bands relative to the monoclinic zirconia (223-233-305-333-345-378-475-505-534-618) are identified even at 900 °C for the single zirconia sample. None of these bands are present for ZrO_2–Al_2O_3 after

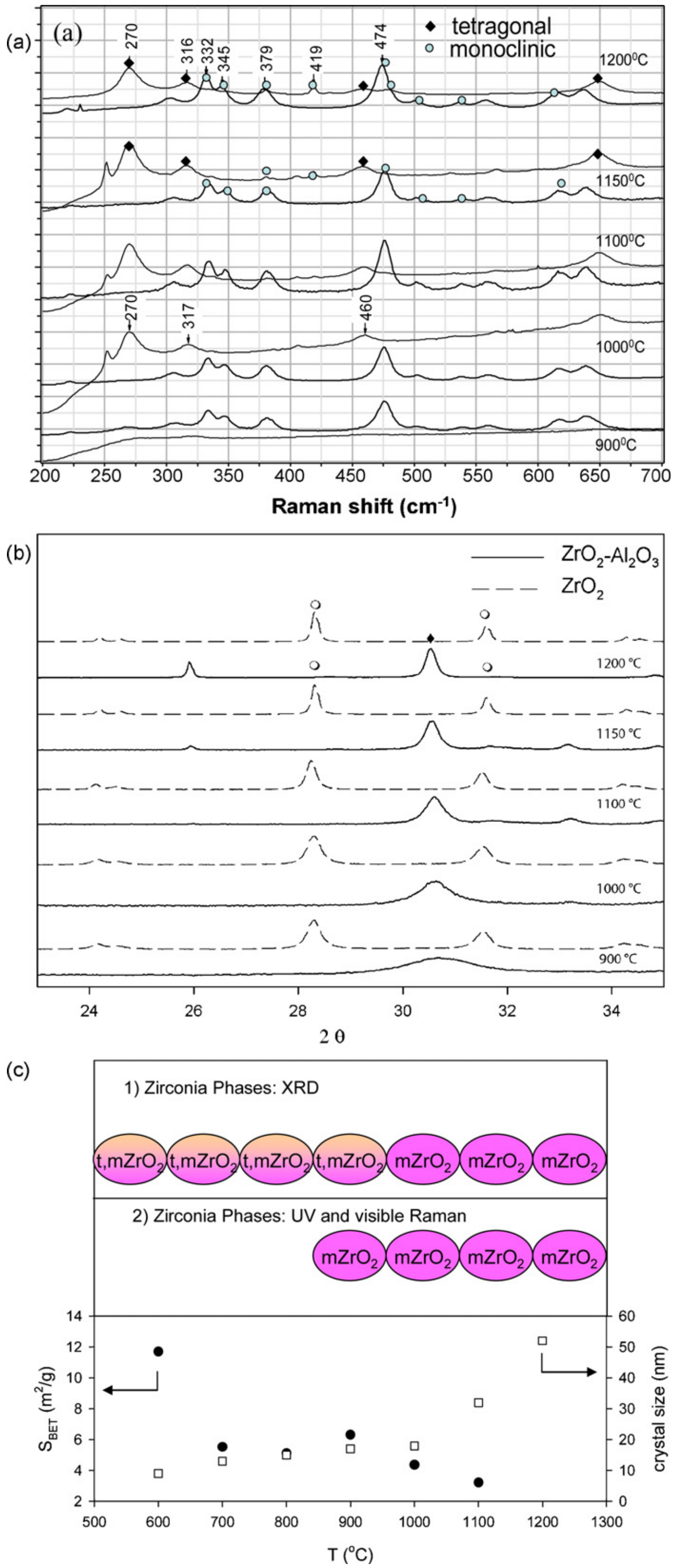

Fig. 4. (a) ZrO_2 phases in ZrO_2–Al_2O_3 nanocomposite (solid line) and ZrO_2 (dashed line) after 900, 1000, 1100 and 1200 °C calcination temperatures under UV-Raman. ♦, t-ZrO_2; ○, m-ZrO_2 (laser excitation at 325 nm). (b) ZrO_2–Al_2O_3 nanocomposite (solid line) and ZrO_2 (dashed line) after different calcination temperatures under XRD. ♦, t-ZrO_2; ○, m-ZrO_2. (c) Comparison of the surface area (●) values with the crystal size for zirconia (□) for the different calcination temperatures. Results are compared with the different phases observed according to XRD and Raman.

calcination at 1100 °C. Only the tetragonal phase is clearly identified thanks to their four broad peaks at about 270, 315, 460 and 650 cm^{-1} [20,32,35]. Regarding the XRD results, for the ZrO_2 sample alone, the m-ZrO_2 is observed even at a calcination temperature of 600 °C, whereas the transition from t-ZrO_2 to m-ZrO_2 is delayed to 1100 °C for the nanocomposite sample. As already reported, metastable phases such as the tetragonal or the cubic zirconia phases can be obtained when the crystallite particle size is below a critical size which is strongly dependent of a very high surface energy [34,37]. The relative surroundings offered by alumina are clearly helpful for stabilizing such a phase and avoiding substantial agglomeration or partial sintering among the nanocrystals. The relative intensity of the bands related to the monoclinic and tetragonal phases indicate that even at the higher heating treatment, the predominant phase is the tetragonal. As expected the contribution of the monoclinic phase is increased with the calcination temperature, as suggested by the stronger peaks related to it at 1200 °C. Therefore, the tetragonal phase of ZrO_2 on alumina can be stabilized by introduction of Al_2O_3 at high temperatures, even at 1200 °C.

The evolution of the crystal size with temperature was studied using the TOPAS program applying the Pawley method [30]. The results are presented in Fig. 2c for the nanocomposite, and in Fig. 4c for the ZrO_2 alone as a function of the calcination temperature. With the introduction of the alumina the crystal size growth for the ZrO_2 is delayed to some degree, probably due to increase of the diffusion barrier for phase transformation [12].

3.4. *CeO_2 phase in CeO_2–Al_2O_3 nanocomposite and CeO_2 nanoparticles*

After calcination at different temperatures, the CeO_2 on the CeO_2–Al_2O_3 nanocomposite shows a strong and sharp peak at ca. 460 cm^{-1} in the Raman spectra due to the F_{2g} Raman active mode of the cubic fluorite structure [6,7,38–43]. With the increased heating treatment a shoulder appears between 500 and 620 cm^{-1}, as shown in Fig. 5a, which is related to the location of the zone-center longitudinal optical phonon mode [6,39]. This band is often linked to oxygen vacancies in the CeO_2 lattice [41,42].

A detailed analysis of the UV Raman spectra as a function of the calcination temperature shows an asymmetrically peak shift to lower energy with decreasing crystals size obtained by means of decreasing the calcination temperature as outlined in Fig. 5a. The evolution of the F_{2g} Raman mode is also presented between 300 and 800 cm^{-1} as shown in the inserted figure in Fig. 5a. The decreased width of the band is found when increasing the calcination temperature. According to Popovic et al. [40] the evolution of the main peak is strongly dependent on the particle size distribution. Asymmetric broad shape of the peaks can be related to the inhomogeneous strain. Sharper and more symmetrical peak indicates to the better crystallization of the CeO_2 [41].

It is observed that lower calcination temperature will lead to the broader shoulder between 500 and 620 cm^{-1}, thus giving a smaller crystal. It has been reported, that by doping CeO_2 with different materials, like Gd_2O_3 [43] or CuO [42], this band becomes important, due to the presence of Ce^{3+} ions in the CeO_2 lattice. Fig. 5b exhibits the UV Raman bands for the CeO_2 samples with for aging temperatures between 900 and 1200 °C, indicating a similar band trend compared to the CeO_2–Al_2O_3. This result is in agreement with the BET surface area and crystal size measurements for the same CeO_2 samples: substantial decrease of BET surface area and increase of the crystal size with increasing the calcination temperature as shown in Figs. 3c and 5c.

Fig. 5d correlates the Raman peak shift as a function of CeO_2 crystal size of both pure CeO_2 and CeO_2–Al_2O_3 composites with for aging temperatures between 900 and 1200 °C. It clearly reveals

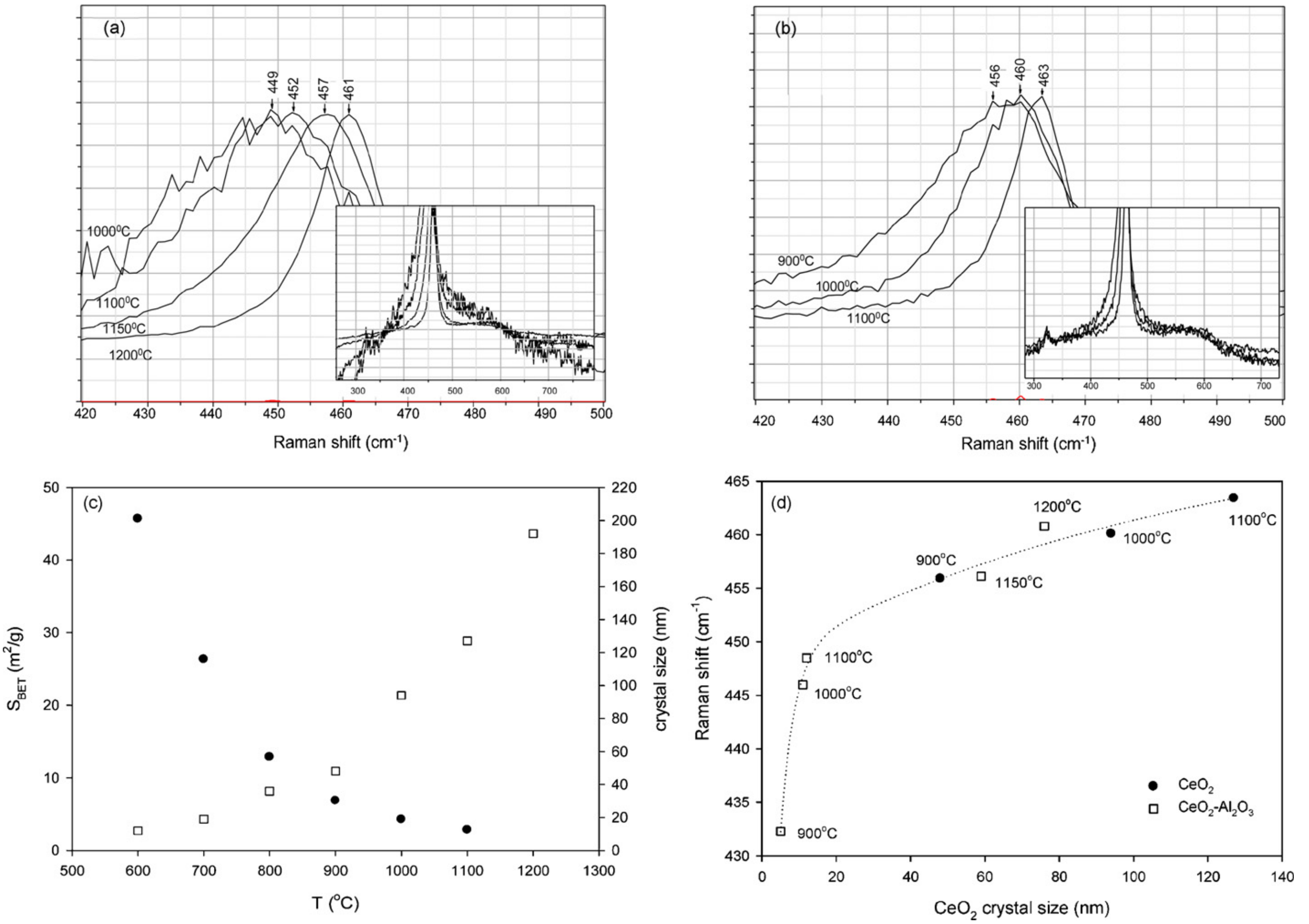

Fig. 5. (a) CeO_2 phase in CeO_2–Al_2O_3 nanocomposite after different calcination temperatures under UV-Raman. In the right corner, UV Raman spectra in the range of 300 and 700 cm^{-1}. (b) CeO_2 phase in CeO_2 after different calcination temperatures under UV-Raman. In the right corner, UV Raman spectra in the range of 300 and 700 cm^{-1}. (c) Comparison of the surface area (●) values with the crystal size for ceria (□) for the different calcination temperatures. c-ceria is found in the whole temperature range according to XRD and Raman. (d) Comparison of the Raman shift evolution with the CeO_2 crystal size values calculated with XRD for the different heat treatments. (●) CeO_2 nanoparticles; (□) CeO_2–Al_2O_3 nanocomposite. Laser excitation 325 nm.

that the Raman peak shift is strongly dependent on the CeO_2 crystal size and the peak shifted to higher energy on the larger CeO_2 crystals, regardless of the support. In good agreement with the modelling study by Spanier, the Raman peak shift is much more pronounced with increasing crystal size on samples with small crystals (less than 20 nm), which is strongly correlated with the vacancy concentration [38]. Spanier et al. analyzed both theoretically and experimentally the factors contributing to the changes in the Raman peak position and peak width of the 464 cm^{-1} peak with nanoparticle size. These include phonon confinement, strain, broadening associated with the size distribution, defects, and variations in phonon relaxation with particle size [38]. The modeling results revealed that the strain is the largest contribution to both Raman peak position shift and peak broadening. Inhomogeneous distribution of the crystal size and the strain can account for much of the broad and asymmetric character of the observed asymmetric line shapes [38]. The strain is normally observed by XRD by means of a significant increase in the lattice parameter with decreasing crystal size. Tsunekawa et al. explained the increase in strain in terms of a reduction in the valence of Ce^{4+} ions to Ce^{3+} ions caused by an increasing molar fraction of oxygen vacancies [44]. Reduced Raman peak position shift after high temperature calcination can be explained by relaxing of strain. Moreover, Fig. 5d clearly shows the stabilizing effect of the alumina to cerium oxides, where the crystal size for the pure CeO_2 oxides calcined at 900 °C is in the same range as the one at a calcination temperature of 1150 °C for the nanocomposites.

It should be mentioned that, the same peak at 464 cm^{-1} due to the F_{2g} Raman active mode of the cubic fluorite structure, can be also observed under visible Raman. However, in agreement with Taniguchi et al. [43], the signal at 464 cm^{-1} is much weaker under visible than under UV. Nevertheless, the shoulder at 620 cm^{-1} is still not detected. It clearly demonstrates that, in our case, UV-Raman improves the sensitivity very much comparing to vis-Raman.

The comparison of the Raman shift evolution with the temperature for both nanocomposites of CeO_2–Al_2O_3 and ZrO_2–Al_2O_3 is reported in Fig. 6. The Raman shift keeps an almost constant value on ZrO_2–Al_2O_3, whereas it is shifted to higher energy values when the calcination temperature is increased on CeO_2–Al_2O_3. The difference cannot be ascribed to the difference in crystal size, and CeO_2 and ZrO_2 have similar crystal size as shown in Figs. 5c and 4c, respectively. It indicates that the reducibility of Ce^{4+} ions is much larger than Zr^{4+} ions. This explains well why CeO_2 is a better material for oxygen storage than ZrO_2.

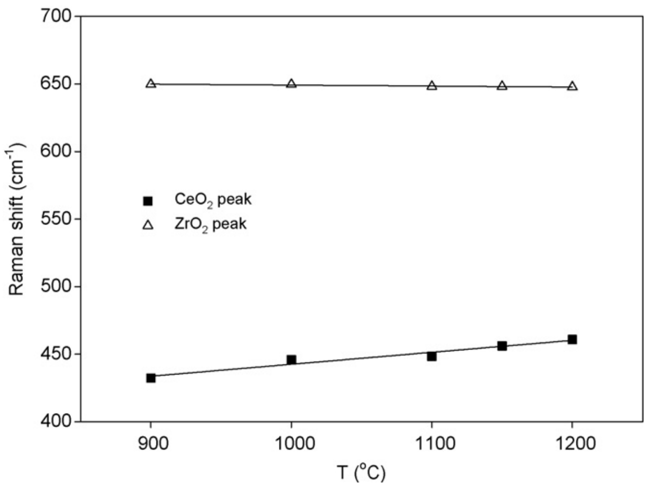

Fig. 6. Comparison of the Raman shift evolution with the temperature for the ZrO_2 and CeO_2–alumina nanocomposites.

4. Conclusions

Combining techniques such as XRD, vis- and UV-Raman is very useful for obtaining a detailed understanding of the phase transition of alumina, ceria and zirconia in their pure oxide and in mixed oxide as composites, and a mechanism for reducing the sintering.

UV-Raman is found to be much more sensitive to the surface region than vis-Raman, enabling a detailed investigation of phase transitions of the second oxides such as ZrO_2 and CeO_2 in the nanocomposite prepared by the nanoparticle-mediated Pechini sol–gel method, which is possibly on the surface of Al_2O_3. This structure makes UV-Raman impossible to detect any reasonably signal of the alumina, which can be studied by visible Raman in a range of 1000–1800 cm^{-1}. The results obtained by Raman have been further confirmed by XRD.

It was found that the modification of the alumina surface can significantly delay the phase transformation and sintering. A synergetic stabilization effect between two oxides such as Al_2O_3 and ZrO_2 or CeO_2 exists: the phase transition and sintering of both oxides is delayed through their role in changing the surface properties. At the calcination temperature of 1000 °C, the surface area follows an order of CeO_2–Al_2O_3 (40 m^2/g) > ZrO_2–Al_2O_3 (22 m^2/g) > Al_2O_3 (11 m^2/g) > ZrO_2 or CeO_2 (4 m^2/g). It clearly illustrates the advantage of the nanocomposites. Different benefits are observed when handling the mixed system compared with the single alumina. The phase transitions of Al_2O_3 and ZrO_2 or CeO_2 in the composites are delayed. The sintering of the metal oxides is reduced to some extent by blocking of the pathway of direct contact between the Al_2O_3 particles. All the results clearly point out a surface-mediated sintering mechanism, and a modification of surface properties can significantly suppress the sintering, which is in good agreement with the observation by Li and co-workers [23]. It further supports Can Li's theory that the surface-mediated sintering mechanism can be common for all the nanoparticles.

The results reveal that the nanocomposites prepared by the nanoparticle-mediated Pechini sol–gel method are highly stable at high temperatures. These materials could be a suitable catalyst support for applications at high temperatures and the application in methane partial oxidation will be reported elsewhere. Moreover, the present study pointed out an effective way to stabilize the tetragonal phase of ZrO_2 at high temperatures which can be extended to many applications. Here we demonstrated also a principle for rational design of composites to stabilize the nanocrystals of CeO_2 with high oxygen vacancy which can be important for many reactions.

Acknowledgement

The financial support from the Norwegian Research Council and Statoil is greatly acknowledged.

References

[1] A. Boumaza, L. Favaro, J. Lédion, G. Sattonnay, J.B. Brubach, P. Berthet, A.M. Huntz, P. Roy, R. Tétot, J. Solid State Chem. 182 (2009) 1171.
[2] A. Gutiérrez-Alejandre, M. González-Cruz, M. Trombetta, G. Busca, J. Ramírez, Micropor. Mesopor. Mater. 23 (1998) 265.
[3] W.D. Kingery, H.D. Bowen, D.R. Uhlmann, Introduction to Ceramics, John Wiley & sons, USA, 1975.
[4] A. Talo, J. Lahtinen, P. Hautojärvi, Appl. Catal. B: Environ. 5 (1995) 221.
[5] J. Kaspar, P. Fornasiero, M. Graziani, Catal. Today 50 (1999) 285.
[6] A. Martinez-Arias, M. Fernandez-Garcia, L.N. Salamanca, R.X. Valenzuela, J.C. Conesa, J. Soria, J. Phys. Chem. B 104 (2000) 4038.
[7] A. Trovarelli, Catalysis by Ceria and Related Materials, World Scientific Publishing Company, London, 2002.
[8] Y. Jia, Y. Hotta, K. Sato, K. Watari, J. Am. Ceram. Soc. 89 (2006) 1103.
[9] Y.S. Wang, C. He, B.J. Hockey, P.I. Lacey, S.M. Hsu, Wear 181–183 (1995) 156.
[10] J. Kaspar, P. Fornasiero, J. Solid State Chem. 171 (2003) 19.
[11] J. Kaspar, P. Fornasiero, N. Hickey, Catal. Today 77 (2003) 419.
[12] S.I. Matsumoto, Catal. Today 90 (2004) 183.
[13] B. Reddy, P. Saikia, P. Bharali, Catal. Surv. Asia 12 (2008) 214.
[14] Z. Wei, H. Li, X. Zhang, S. Yan, Z. Lv, Y. Chen, M. Gong, J. Alloys Compd. 455 (2008) 322.
[15] M.H. Yao, R.J. Baird, F.W. Kunz, T.E. Hoost, J. Catal. 166 (1997) 67.
[16] S. Moreau, M. Gervais, A. Douy, Solid State Ionics 101–103 (1997) 625.
[17] G. Stefanic, S. Music, R. Trojko, J. Alloys Compd. 388 (2005) 126.
[18] S. Cava, S.M. Tebcherani, I.A. Souza, S.A. Pianaro, C.A. Paskocimas, E. Longo, J.A. Varela, Mater. Chem. Phys. 103 (2007) 394.
[19] F. Roelofs, W. Vogelsberger, J. Colloid Interface Sci. 303 (2006) 450.
[20] C. Li, M. Li, J. Raman Spectrosc. 33 (2002) 301.
[21] M. Li, Z. Feng, G. Xiong, P. Ying, Q. Xin, C. Li, J. Phys. Chem. B 105 (2001) 8107.
[22] J. Zhang, M. Li, Z. Feng, J. Chen, C. Li, J. Phys. Chem. B 110 (2005) 927.
[23] J. Zhang, Q. Xu, M. Li, Z. Feng, C. Li, J. Phys. Chem. C 113 (2009) 1698.
[24] Y.-F. Han, F. Chen, Z. Zhong, K. Ramesh, L. Chen, E. Widjaja, J. Phys. Chem. B 110 (2006) 24450.
[25] Y.-F. Han, K. Ramesh, L. Chen, E. Widjaja, S. Chilukoti, F. Chen, J. Phys. Chem. C 111 (2007) 2830.
[26] P.A. Badkar, J.E. Bailey, J. Mater. Sci. 11 (1976) 1794.
[27] B.L. Cushing, V.L. Kolesnichenko, C.J. O'Connor, Chem. Rev. 104 (2004) 3893.
[28] J. Lin, M. Yu, C. Lin, X. Liu, J. Phys. Chem. C 111 (2007) 5835.
[29] E. Smith, G. Dent, Modern Raman Spectroscopy: A Practical Approach, Wiley, England, 2008.
[30] G.S Pawley, J. Appl. Crystallogr. 14 (1981) 357.
[31] T. Horiuchi, Y. Teshima, T. Osaki, T. Sugiyama, K. Suzuki, T. Mori, Catal. Lett. 62 (1999) 107.
[32] D. Gazzoli, G. Mattei, M. Valigi, J. Raman Spectrosc. 38 (2007) 824.
[33] L. Kumari, G.H. Du, W.Z. Li, R.S. Vennila, S.K. Saxena, D.Z. Wang, Ceram. Int. 35 (2009) 2401.
[34] V. Grover, R. Shukla, A.K. Tyagi, Scripta Mater. 57 (2007) 699.
[35] A. Cabanas, J.A. Darr, E. Lester, M. Poliakoff, J. Mater. Chem. 11 (2001) 561.
[36] A. Gulino, S. La Delfa, I. Fragala, R.G. Egdell, Chem. Mater. 8 (1996) 1287.
[37] R.D. Purohit, S. Saha, A.K. Tyagi, Mater. Sci. Eng. B 130 (2006) 57.
[38] J.E. Spanier, R.D. Robinson, F. Zhang, S.-W. Chan, I.P. Herman, Phys. Rev. B 64 (2001) 245407.
[39] J.Z. Shyu, W.H. Weber, H.S. Gandhi, J. Phys. Chem. 92 (2002) 4964.
[40] Z.V. Popovic, Z. Dohcevic-Mitrovic, A. Cros, A. Cantarero, J. Phys. Condens. Matter (2007) 496209.
[41] B.M. Reddy, K.N. Rao, G.K. Reddy, A. Khan, S.-E. Park, J. Phys. Chem. C 111 (2007) 18751.
[42] L. Li, Y. Zhan, Q. Zheng, Y. Zheng, C. Chen, Y. She, X. Lin, K. Wei, Catal. Lett. 130 (2009) 532.
[43] T. Taniguchi, T. Watanabe, N. Sugiyama, A.K. Subramani, H. Wagata, N. Matsushita, M. Yoshimura, J. Phys. Chem. C 113 (2009) 19789.
[44] S. Tsunekawa, K. Ishikawa, Z.-Q. Li, Y. Kawazoe, Y. Kasuya, Phys. Rev. Lett. 85 (2000) 3440.